



# An antenna/spacer/reflector based Au/BiVO<sub>4</sub>/WO<sub>3</sub>/Au nanopatterned photoanode for plasmon-enhanced photoelectrochemical water splitting

Bin Chen<sup>a</sup>, Zhuo Zhang<sup>a</sup>, Minki Baek<sup>a</sup>, Sangkuk Kim<sup>a</sup>, Wooyul Kim<sup>b</sup>, Kijung Yong<sup>a,\*</sup>

<sup>a</sup> Surface Chemistry Laboratory of Electronic Materials, Department of Chemical Engineering, Pohang University of Science and Technology (POSTECH), Pohang 37673, Republic of Korea

<sup>b</sup> Department of Chemical and Biological Engineering, College of Engineering, Sookmyung Women's University, Seoul 04310, Republic of Korea

## ARTICLE INFO

### Keywords:

Photoelectrochemical water splitting  
BiVO<sub>4</sub>  
Au  
Nanopatterned photoanode  
Plasmonic effects

## ABSTRACT

BiVO<sub>4</sub> is one of the most promising photoanodes for photoelectrochemical (PEC) water splitting. However, BiVO<sub>4</sub> is limited by less-than-unity efficiencies of light absorption and charge separation due to a trade-off between the long penetration depth of photons and relatively short length carrier diffusion. Here, an antenna/spacer/reflector based Au/BiVO<sub>4</sub>/WO<sub>3</sub>/Au nanopatterned photoanode is designed by integrating ultrathin BiVO<sub>4</sub> layer between two kinds of Au nanospheres (NSs) with different sizes. The large underlying nanopatterned Au NSs serve as current collector and back reflector to reflect the incident light by Bragg reflection of the highly ordered Au NSs array, while the small surface Au NSs act as antennas to absorb the incident and reflected light, which concentrates the light energy to the BiVO<sub>4</sub> layer. Moreover, a strong electromagnetic field is created in the BiVO<sub>4</sub> spacer due to the coupling interaction between the reflector and antenna, which promotes the charge separation of BiVO<sub>4</sub>. Based on this unique antenna/spacer/reflector structure, the ultrathin BiVO<sub>4</sub> of only 70 nm achieves a photocurrent density of 1.31 mA/cm<sup>2</sup> at 1.23 V<sub>RHE</sub>, which demonstrates an impressive 3.23 fold enhancement by the combined plasmonic effects, and it further increases to 1.97 mA/cm<sup>2</sup> after depositing FeOOH catalyst. The strategy paves a way for other semiconductors and thin-film optoelectronic devices to improve their performance.

## 1. Introduction

Photoelectrochemical (PEC) water splitting has been regarded as one of the most promising green technologies to convert solar energy directly into hydrogen as storable and carbon-free fuel [1,2]. Since the pioneering work of TiO<sub>2</sub>-based photoelectrodes for water splitting [3], various semiconductor materials, such as ZnO [4–6], WO<sub>3</sub> [7,8], Cu<sub>2</sub>O [9], Fe<sub>2</sub>O<sub>3</sub> [10–12], BiVO<sub>4</sub> [13–16], and others [17,18], have been widely studied for PEC water splitting. Among these semiconductors, monoclinic BiVO<sub>4</sub> is one of the most promising performers due to its relatively narrow band gap of 2.4 eV, suitable valence band position for O<sub>2</sub> evolution, and favorable conduction band (CB) edge position very near the thermodynamic hydrogen evolution potential [19–23]. However, the practical photocurrent density remains too low, because BiVO<sub>4</sub> suffers from its less-than-unity efficiencies of light absorption ( $\eta_{\text{abs}}$ ), charge separation and transport ( $\eta_{\text{sep}}$ ), and charge transfer at the semiconductor/electrolyte interface ( $\eta_{\text{trans}}$ ). Among these efficiencies, the value of  $\eta_{\text{trans}}$  has been significantly increased by improving the slow hole transfer kinetics of oxygen evolution via surface modifications of BiVO<sub>4</sub> with oxygen evolution reaction (OER) catalysts (such as CoPi,

NiOOH, and FeOOH) [19,24]. Nevertheless, the values of  $\eta_{\text{abs}}$  and  $\eta_{\text{sep}}$  are still low due to a trade-off between the long penetration depth of photons and the relatively short length carrier diffusion, which results in severe recombination of photogenerated electron-hole pairs in the bulk phase [25]. In this regard, the BiVO<sub>4</sub> films for photoanodes should be extremely thin to prevent the electron-hole recombination, while a relatively thicker layer is required to capture more solar light. To resolve this mismatch between the carrier diffusion length and light absorption depth, engineering their nanostructures [26,27], impurity doping [22,27], and heterojunctions formation [28,29] have been extensively studied to improve the PEC performance of BiVO<sub>4</sub>. However, the practical water oxidation photocurrent of BiVO<sub>4</sub>-based photoanodes is still inferior to that of theoretical prediction.

Recently, plasmonic metal nanoparticles (NPs) have been widely studied because they can concentrate the light energy and promote the charge separation, which provides a new opportunity to improve the efficiency of solar energy conversion [30,31]. When the frequency of the incident light matches well with the inherent frequency of the free electrons on the metal NP surface, it will lead to a collective oscillation of the free electrons, commonly known as localized surface plasmon

\* Corresponding author.

E-mail address: [kyong@postech.ac.kr](mailto:kyong@postech.ac.kr) (K. Yong).

resonance (LSPR) [31–33]. LSPR of NPs gives rise to both strong absorption and scattering of the incident light. It should be noted that the size of plasmonic NPs is a predominant factor affecting light absorption and scattering properties [34]. Specifically, the scattering effect is much weaker than absorption effect when the NP size is small (less than 60 nm), while, for larger NPs, the scattering effect dominates [33,34]. According to the position of plasmonic NPs in the heterojunction formed with semiconductors, the reported research about plasmonic enhancement can be divided into two categories. On one hand, most reported research focused on absorption effects by decorating relatively small plasmonic NPs on the surface of semiconductors to extend the light absorption range (especially for semiconductors with large bandgap) [6,35], hot-electron-injection effect [36], or plasmon-induced resonance energy transfer (PIRET) process [33,37]. Alternatively, plasmonic NPs or nanopatterned substrates beneath the semiconductors can act as a back reflector (scattering effect) for resonant light trapping to increase the total transport pathway of photons within the semiconductor, while the enhanced electromagnetic field created by plasmonic NPs can also promote light absorption and charge separation of semiconductors [38–41]. Although studies of plasmonic NPs located on the surface of semiconductors or beneath the semiconductors have been conducted respectively, little research combines these two kinds of metal NPs with LSPR to simultaneously utilize the effects of both light absorption and scattering in the backward direction for PEC water splitting.

Herein, we present a multifunctional plasmon-enhanced PEC water splitting of an ultrathin BiVO<sub>4</sub> photoanode in an antenna/spacer/reflector based Au/BiVO<sub>4</sub>/Au nanostructure by integrating two types of Au nano-spheres (NSs) with quite different sizes (as shown schematically in Fig. 1a and b), via a combinatorial process of polystyrene (PS) template-assisted growing large (~245 nm) Au NSs on F:SnO<sub>2</sub> coated glass (FTO), followed by magnetron sputtering Au film (80–100 nm) to fabricate a nanopatterned Au NSs/film (denoted as Au-bottom), subsequently spin coating a thin WO<sub>3</sub> layer (10–15 nm, hole blocking layer) and BiVO<sub>4</sub> layer (~70 nm, light-absorber) as the photoanode, and then decorating small Au NSs (~20 nm, denoted as Au-surface), as shown in Fig. 1c. The large Au NSs combined with Au film (Au-bottom) can serve as current collector and light reflector, which can scatter the incident light in the backward direction by Bragg reflection of the highly ordered Au NSs array, leading to both resonant light trapping and light retrapping (Fig. 1a). The thin WO<sub>3</sub> layer serves as a selective electron transport layer to block the hole injection into the Au-bottom (Fig. 1b) [41]. The small Au NSs (Au-surface) decorated on BiVO<sub>4</sub> can act as antennas to harvest both the incident and reflected light. Additionally, theoretical simulations demonstrate that a favorable interplay between the reflector and antenna has been created in the spacer (BiVO<sub>4</sub> layer), due to the strong coupling effect of electromagnetic field created by both of the Au nanostructures, which is also known as hot spot [32,33]. The strongly enhanced electric field can promote the optical absorption and charge separation for BiVO<sub>4</sub>. Similar metal-spacer-metal sandwich structures have presented promising characteristics for surface-enhanced Raman scattering and infrared spectroscopy applications [30,42]. Based on this unique antenna/spacer/reflector structure, both the efficiencies of light absorption and charge separation of BiVO<sub>4</sub> photoanodes were simultaneously increased. Significantly, the ultrathin BiVO<sub>4</sub> photoanode (only 70 nm) located between the Au-bottom and Au-surface demonstrates a photocurrent density of 1.31 mA/cm<sup>2</sup> at 1.23 V vs reversible hydrogen electrode (V<sub>RHE</sub>), and it is further increased to 1.97 mA/cm<sup>2</sup> after coating FeOOH layer as OER catalyst, which is comparable or even better than the results of pure BiVO<sub>4</sub> films (200 nm or thicker) in the literature.

## 2. Experimental section

### 2.1. Fabrication of the Au/BiVO<sub>4</sub>/Au nanopatterned photoanode

#### 2.1.1. Materials

Monodisperse PS spheres with diameters of 500 nm in aqueous suspension (2.5 wt%) were purchased from Alfa Aesar Corporation. Tungstic acid (H<sub>2</sub>WO<sub>4</sub>, 99%), poly(vinylalcohol) (PVA, 89,000), bismuth nitrate pentahydrate (Bi(NO<sub>3</sub>)<sub>3</sub>·5H<sub>2</sub>O, 98%), vanadyl acetylacetonate (VO(acac)<sub>2</sub>, 98%), acetic acid (99.7%), acetyl acetone (99%), ferric chloride (FeCl<sub>3</sub>·6H<sub>2</sub>O, 99%), urea (98%), auric chloride acid (HAuCl<sub>4</sub>·4H<sub>2</sub>O, 99%) and trisodium citrate (99%) were obtained from Sigma-Aldrich Chemicals.

#### 2.1.2. Fabrication of the bottom Au NSs array on FTO

To begin with, the PS monolayer colloidal array was fabricated on a cleaned glass slide by a reported air/water interfacial self-assembly method [43]. Briefly, the PS sphere suspension was diluted with alcohol at a volume ratio of 1:1.2 by ultrasonication for 15 min, and the glass slide was cleaned with acetone, alcohol, 98% H<sub>2</sub>SO<sub>4</sub>/H<sub>2</sub>O<sub>2</sub> (3:1), H<sub>2</sub>O/NH<sub>3</sub>·H<sub>2</sub>O/H<sub>2</sub>O<sub>2</sub> (5:1:1), and deionized water (DI water), respectively. Then, an appropriate amount of DI water was dropped onto the glass slide, and the PS suspension was added slowly on the water surface, drop by drop, thus, a hexagonally patterned PS monolayer colloidal array was prepared by self-assembly at the air-water interface. After the evaporation of water at room temperature, the PS monolayer array was transferred onto an FTO coated glass from the glass slide using the water surface as a medium [43], as shown in Fig. 1c (i). Next, a thin layer of Au (~20 nm) was coated on the PS sphere array using radio frequency (RF) magnetron sputtering for 2 min under argon protection (Fig. 1c (ii)). Subsequently, the Au film coated PS colloidal array was annealed at 550 °C for 2 h in air, during which the PS spheres were removed, meanwhile, the thin Au films on PS spheres melted and in situ formed spherical particles driven by the principle of surface free energy minimum. Therefore, hexagonally patterned Au NS arrays were fabricated on FTO glass (Fig. 1c (iii)). Finally, a thick Au film (80–100 nm) was deposited on the surface of Au NPs/FTO by magnetron sputtering, resulting in a continuous and nano-patterned film (Au-bottom, Fig. 1c (iv)).

#### 2.1.3. Synthesis of WO<sub>3</sub>/BiVO<sub>4</sub> layer

The ultrathin WO<sub>3</sub> and BiVO<sub>4</sub> layers were deposited on the Au-bottom by a sol-gel spin coating method. For the WO<sub>3</sub> coating solution, 0.625 g of H<sub>2</sub>WO<sub>4</sub> and 0.25 g of PVA were sequentially dissolved in 10 mL of 30 wt% H<sub>2</sub>O<sub>2</sub> at 80 °C while stirring [8]. For the BiVO<sub>4</sub> coating solution, 0.05 M Bi(NO<sub>3</sub>)<sub>3</sub>·5H<sub>2</sub>O and 0.05 M VO(acac)<sub>2</sub> were dissolved in 20:1 (v/v) acetic acid/acetyl acetone [41]. Using the above coating solution, each film was deposited by spin coating at a spin speed of 4000 rpm for 40 s and then annealed in air at 500 °C for 15 min in air. The film thickness was controlled by tuning the total spin coating times. After the last spin coating process for each layer, the sample was annealed at 500 °C for 2 h to produce a uniform WO<sub>3</sub>/BiVO<sub>4</sub> layer coating on Au-bottom film (Fig. 1c (v)).

#### 2.1.4. Synthesis and decoration of the surface Au NSs

The 20-nm Au NSs were synthesized by reducing HAuCl<sub>4</sub> with trisodium citrate [44]. Briefly, 100 mL of 0.01% HAuCl<sub>4</sub> solution was heated to boil under continuous stirring (500 RPM), then 3 mL of 1% trisodium citrate was added, and boiling was continued for 10 min. The as-synthesized Au NPs were dropped onto the top surface of the photoanode, and the whole sample was kept in an oven at 40 °C until dry to decorate Au NPs onto WO<sub>3</sub>/BiVO<sub>4</sub>/Au (Fig. 1c (vi)).

#### 2.1.5. Hydrothermal deposition of FeOOH catalyst

Finally, the FeOOH catalyst was deposited on the as-prepared photoanode by a simple modified hydrothermal method [19,45]. First,

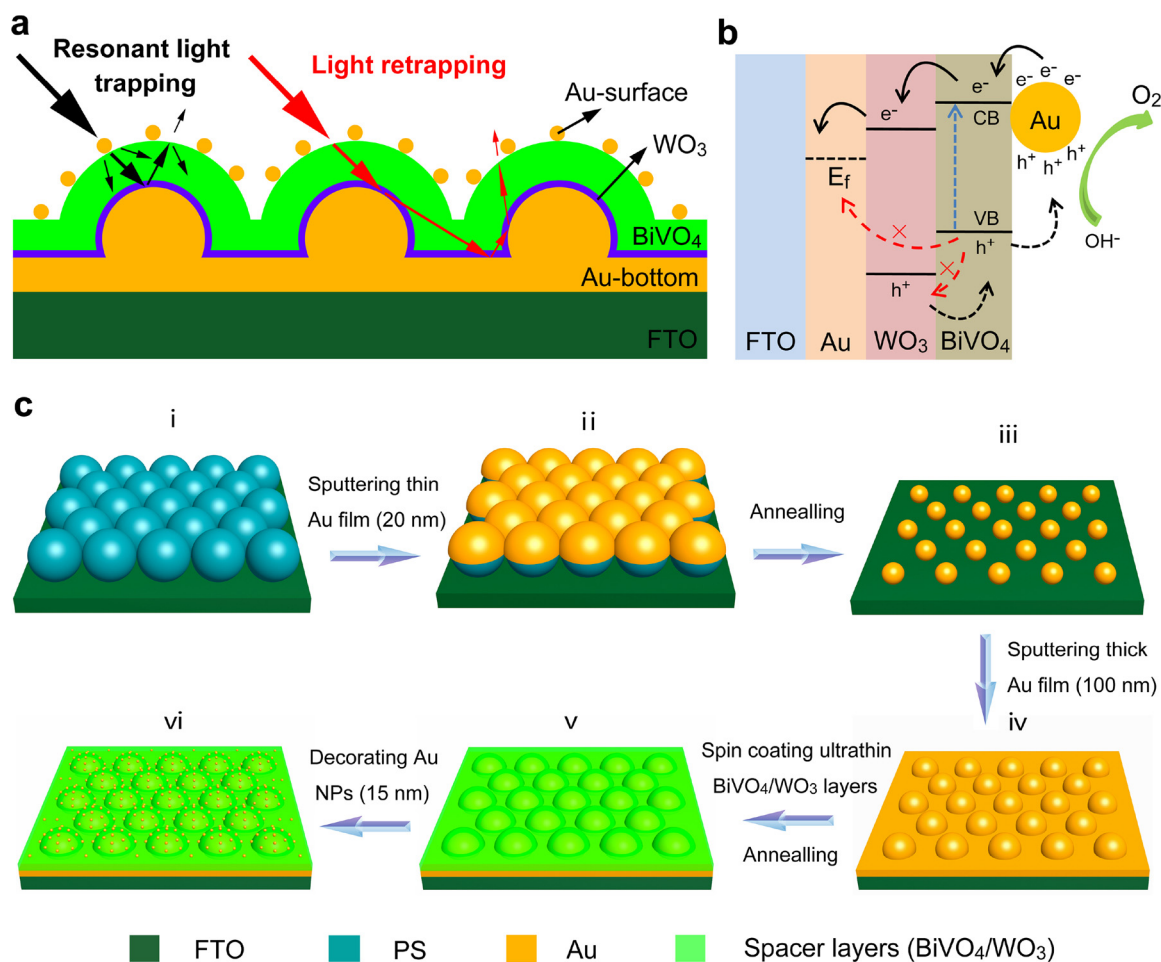


**Fig. 1.** Schematic illustration of the design rationales, energy diagram, and fabrication of the antenna/spacer/reflector based Au-surface/BiVO<sub>4</sub>/WO<sub>3</sub>/Au-bottom nanopatterned photoanode. (a) Schematic illustration of the design rationales for resonant light trapping and light retrapping. (b) Energy diagram for PEC water splitting under solar light irradiation. (c) Schematic for the fabrication of the antenna/spacer/reflector based photoanode.

0.3 M FeCl<sub>3</sub>·6H<sub>2</sub>O and 0.045 M urea were dissolved in DI water in a bottle by magnetic stirring. Then, the as-prepared photoanodes were immersed in the precursor solution and leaned against the sidewall. The bottle was heated in an oven at 100 °C for 30 min. Then, the samples were rinsed with DI water and dried in air.

## 2.2. Characterizations

The morphology and structure were characterized by a field-emission scanning electron microscope (FE-SEM, JSM-7800 F Prime, JEOL, operated at 5.0 kV), and a high-resolution scanning transmission electron microscope (HR-STEM, JEM-2200FS with Cs-corrector, JEOL, operated at 200 kV). The crystalline structures were observed by X-ray diffraction (XRD, D/MAX-2500, Rigaku) with Cu K $\alpha$  radiation (40 kV, 100 mA). The transmittance (T) and reflectance (R) spectra of the as-prepared photoanodes were carried out with a UV–vis spectrometer (Lambda 750S, PerkinElmer), and the absorption (A) was calculated by using the formula:  $A = 100 - T - R$ . Photoluminescence (PL) spectra were recorded by a fluorescence spectrometer (RF-5301, Shimadzu) with the excitation wavelength of 325 nm at room temperature.

## 2.3. Photoelectrochemical measurements

All the PEC measurements were performed by a potentiostat system (Potentiostat/Galvanostat, model 263A, EG&G Princeton Applied Research) using a three-electrode cell with a Pt counter electrode and an Ag/AgCl reference electrode. A 0.5 M Na<sub>2</sub>SO<sub>4</sub> aqueous solution

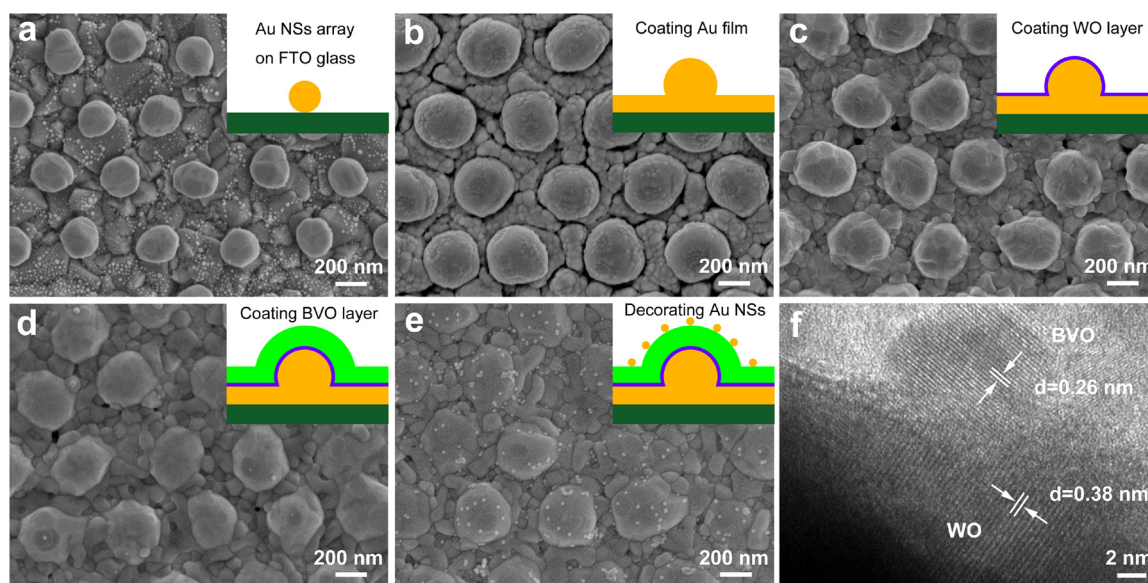
without any hole scavenger (pH = 6.5) was used as the electrolyte. The working electrode was illuminated from the front side under one sun condition ( $100 \text{ mW cm}^{-2}$ ) with a solar simulator (AM 1.5 G filtered, 91160, Oriel). The as-measured potentials versus Ag/AgCl ( $E_{\text{Ag/AgCl}}$ ) were converted to the RHE scale ( $E_{\text{RHE}}$ ) according to the Nernst equation:  $E_{\text{RHE}} (\text{volt}) = E_{\text{Ag/AgCl}} (\text{volt}) + 0.059 (\text{volt}) \times \text{pH} + 0.197 (\text{volt})$ . For the photocurrent density–voltage ( $J-V$ ) curves, the applied voltage was swept linearly at a scan rate of 10 mV/s. Incident photocurrent conversion efficiency (IPCE) measurements were carried out by a 300 W Xe lamp (66 905, Oriel Instruments) with a monochromator (74-004, Oriel Cornerstone 130 1/8 m) at a potential of 1.23 V<sub>RHE</sub>. The intensity of the monochromatic light was measured by a calibrated silicon photodiode. Electrochemical impedance spectroscopy (EIS) measurements were performed at 1.23 V<sub>RHE</sub>, and an amplitude of 10 mV was applied to the electrode with frequency range of 100 kHz–0.1 Hz.

## 3. Results and discussion

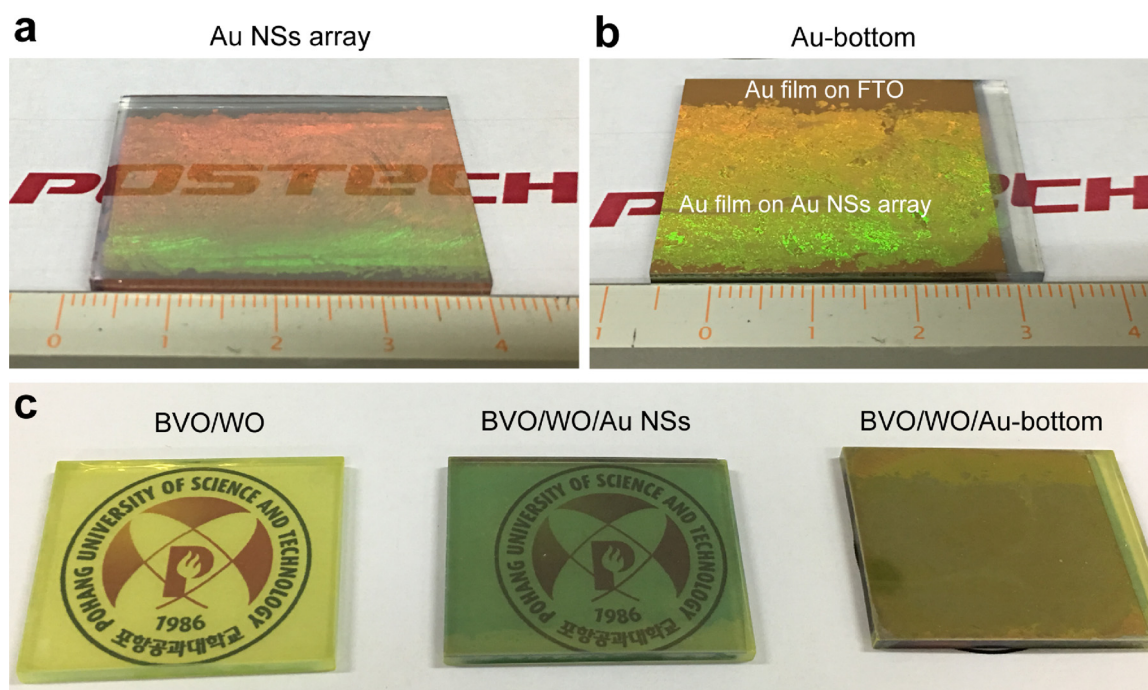
### 3.1. Morphology and structure

Fig. 2 shows the structural characterizations of the photoanodes obtained after different fabrication steps, while the corresponding photographs are shown in Fig. S1. First, highly ordered and hexagonally patterned arrays of Au NSs were achieved by a PS template-assisted method, as demonstrated in SEM image (Fig. 2a). To generate LSPR modes in visible wavelengths, we patterned the Au NSs in periodic lattices with 500-nm pitch. The Au NSs show a smooth surface, with a





**Fig. 2.** Structural characterizations of the photoanodes after different fabrication steps. (a) SEM image of the Au NSs array on FTO glass. (b) SEM image of nano-patterned Au-bottom achieved by coating Au film on Au NSs array. (c) SEM image of  $\text{WO}_3/\text{Au}$ -bottom achieved by spin coating  $\text{WO}_3$  layer on Au-bottom. (d) SEM image of  $\text{BiVO}_4/\text{WO}_3/\text{Au}$ -bottom. (e) Au-surface/ $\text{BiVO}_4/\text{WO}_3/\text{Au}$ -bottom. (f) HRTEM image of  $\text{BiVO}_4/\text{WO}_3/\text{Au}$ -bottom.



**Fig. 3.** Photographs of the different photoanodes. (a) Au NSs array on FTO glass. (b) Au-bottom on FTO glass, and the top side of the sample is Au film directly deposited on bare FTO. (c)  $\text{BiVO}_4/\text{WO}_3$  on bare FTO,  $\text{BiVO}_4/\text{WO}_3$  on Au NSs array, and  $\text{BiVO}_4/\text{WO}_3$  on Au-bottom. (For interpretation of the references to color in the text, the reader is referred to the web version of this article).

predesigned and uniform diameter of approximately 245 nm. The diameters could be tailored by tuning the sputtering thickness of Au film on the PS template. The photographs (Figs. S1a and 3 a) show the Au NSs array on FTO presented a large-scale uniformity (more than  $3.5\text{ cm} \times 2.5\text{ cm}$ ), and the strong iridescent color originated from the Bragg reflection of the highly ordered Au NSs array [43], indicating that the Au NSs array can effectively scatter the incident light in the backward direction. Compared to bare Au NSs that exhibit extremely confined localized plasmon resonances, the continuous and nanostructured Au substrates sustain surface plasmon modes whose evanescent fields exhibit much longer decay lengths [10]. Therefore, a thick

Au film was deposited on the surface of the Au NSs/FTO by magnetron sputtering. As shown in Fig. 2b, the diameters of Au NSs increase to 400 nm, and the bottoms of Au NSs are immersed in the Au film, resulting in a continuous and nanopatterned film (Au-bottom). The cross-sectional SEM images also show a large-scale uniformity of the nano-patterned Au-bottom, and the thickness of the Au-bottom was approximately 80–100 nm (Fig. S2). The Au-bottom serves as the back electron collector and light reflector, and Au was chosen due to its high electrical conductivity and good chemical stability during the following fabrication conditions of  $\text{WO}_3$  and  $\text{BiVO}_4$ . Compared to the Au NSs array (Figs. S1a and 3a), the Au-bottom (Figs. S1b and 3b) displayed a

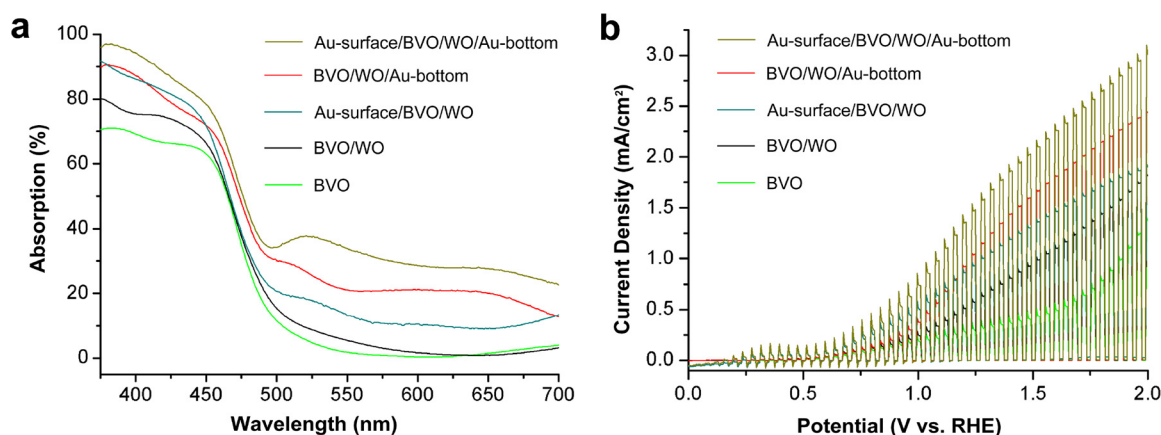


**Fig. 4.** Optical and PEC performances of the different photoanodes. (a) Light absorption and (b)  $J-V$  curves measured under chopped light (AM 1.5G) of BiVO<sub>4</sub>, BiVO<sub>4</sub>/WO<sub>3</sub>, Au-surface/BiVO<sub>4</sub>/WO<sub>3</sub>, BiVO<sub>4</sub>/WO<sub>3</sub>/Au-bottom, and Au-surface/BiVO<sub>4</sub>/WO<sub>3</sub>/Au-bottom in 0.5 M Na<sub>2</sub>SO<sub>4</sub> solution without any hole scavenger.

stronger iridescent color, and nearly all light was absorbed and scattered. Additionally, the ordinary Au films directly deposited FTO (as shown on the top side of the sample in Fig. 3b) do not have any iridescent color, which means this unique scattering phenomenon is created by the Bragg scattering of patterned nanostructure array.

Next, a thin WO<sub>3</sub> layer was spin coated onto the surface of Au-bottom/FTO (Fig. 2c). After coating the WO<sub>3</sub> layer for one time, the surface of Au-bottom becomes smoother. The resultant substrate still maintained its original nanopatterned feature with a very small size change, being indicative of the WO<sub>3</sub>-layer homogeneity and ultrathin in nature. To show the thickness of WO<sub>3</sub> layer, a thicker WO<sub>3</sub> layer was coated on the Au-bottom by the same spin coating conditions for two times. As shown in the cross-sectional SEM image (Fig. S3a), double layer structures could be seen clearly, which demonstrates the average thicknesses of Au film and WO<sub>3</sub> layer were approximately 80 nm and 25 nm, respectively. Therefore, it can be inferred that the thickness of WO<sub>3</sub> layer coated for one time is about 10–15 nm. To obviate the disturbances of Au film, WO<sub>3</sub> layer was directly coated on Au NSs array for one time, as shown in Fig. S4. After coating the WO<sub>3</sub> layer, the average diameter of NSs increased from 245 nm to 271 nm, which also implied the thicknesses WO<sub>3</sub> layer coated for one time was approximately 10–15 nm. The corresponding elemental mappings using energy dispersive spectrometer (EDS) reveal the homogeneous spatial distribution of both W and O elements on the substrate, implying the surface of Au-bottom was completely and uniformly coated by the WO<sub>3</sub> layer (Fig. S5). The photograph (Fig. S1c) shows there is a little change after coating WO<sub>3</sub>. It should be noted that the Au-bottom film demonstrates minimal morphology changes during the annealing process, implying the Au-bottom film was not melted as in the case of the formation of Au NSs transferred from the thin Au layer (20 nm) on PS template. The primary reasons are that the Au-bottom film is much thicker, and the annealing temperature is also 50 °C below that in the formation of Au NSs. Then, a thin BiVO<sub>4</sub> film was grown on the WO<sub>3</sub>/Au-bottom substrate by spin coating for three times, as shown in Fig. 2d. Elemental mapping images demonstrate the homogeneous spatial distribution of Bi, V, and O elements, which indicates the BiVO<sub>4</sub> layer could be uniformly coated on the WO<sub>3</sub>/Au-bottom, leading to BiVO<sub>4</sub>/WO<sub>3</sub>/Au multi-layered structure (Fig. S6). As shown in the cross-sectional SEM images (Fig. S3b–d), the multi-layered structure could be seen clearly, and the BiVO<sub>4</sub> layer thickness could be controlled by the spin coating times. Typically, the average thickness of BiVO<sub>4</sub> layer by spin coating for three times was about 70 nm (Fig. S3c). The photograph (Fig. S1d) shows the BiVO<sub>4</sub>/WO<sub>3</sub>/Au-bottom displayed a yellow-green color, and the iridescent color from Au-bottom disappeared, implying the scattered and reflected light was absorbed by the semiconductor layers.

Then, much smaller Au NSs were synthesized by reducing HAuCl<sub>4</sub> with trisodium citrate. The TEM images demonstrate that Au NSs have a

homogeneous morphology with a similar diameter approximately 20 nm (Fig. S7). The as-prepared Au NSs were dropped onto the top surface of BiVO<sub>4</sub>/WO<sub>3</sub>/Au-bottom substrate, resulting in a unique metal-semiconductor-metal sandwich structure (Au-surface/BiVO<sub>4</sub>/WO<sub>3</sub>/Au-bottom). As shown in Fig. 2e, the Au NSs were uniformly distributed on the substrate. The densities of Au NSs could be controlled by tuning the concentration of Au NSs colloidal solution. The photograph (Fig. S1d) shows the color of sample becomes darker. The crystallinities of the BiVO<sub>4</sub>/WO<sub>3</sub> layer-built structures were investigated by high-resolution TEM (HRTEM), in which BiVO<sub>4</sub> and WO<sub>3</sub> could be distinguished by different lattice fringes (Fig. 2f). The corresponding lattice spacings are about 0.26 nm and 0.38 nm, which correspond to the (200) plane of the monoclinic BiVO<sub>4</sub> and (002) plane of monoclinic WO<sub>3</sub>, respectively [26]. A cross-sectional SEM image of Au-surface/BiVO<sub>4</sub>/WO<sub>3</sub>/Au-bottom on FTO (Fig. S8) shows that the thickness of the whole antenna/spacer/reflector based photoanode was only approximately 200 nm. The crystalline structures of the Au-bottom, WO<sub>3</sub> layer, BiVO<sub>4</sub> layer, and BiVO<sub>4</sub>/WO<sub>3</sub>/Au-bottom on FTO glasses were also characterized by XRD, as shown in Fig. S9. As expected, monoclinic WO<sub>3</sub> (JSPDF: #00-005-0363) and monoclinic BiVO<sub>4</sub> (JSPDF: #01-75-1867) are the only phases detected in XRD measurements.

### 3.2. Photoelectrochemical performances

To evaluate the capability of light absorption for PEC applications, UV–vis absorption spectra of the five samples, bare BiVO<sub>4</sub>, BiVO<sub>4</sub>/WO<sub>3</sub>, Au-surface/BiVO<sub>4</sub>/WO<sub>3</sub>, BiVO<sub>4</sub>/WO<sub>3</sub>/Au-bottom, and Au-surface/BiVO<sub>4</sub>/WO<sub>3</sub>/Au-bottom were measured (Fig. 4a). The light absorption edge of bare BiVO<sub>4</sub> on FTO glass is approximately 520 nm, which matches the BiVO<sub>4</sub> bandgap of 2.4 eV. BiVO<sub>4</sub>/WO<sub>3</sub> shows an enhanced light absorption, mainly in the light spectrum below 470 nm, due to the broader bandgap of WO<sub>3</sub>. After coating the small Au NSs (Au-surface) on BiVO<sub>4</sub>/WO<sub>3</sub>, there was a broad absorption peak near 525 nm which originated from the LSPR peak of the Au NSs. This absorption peak was relatively weak because of the very small sizes (20 nm) and relatively small amount of the coated Au NSs. By combining the Au-bottom underneath BiVO<sub>4</sub>/WO<sub>3</sub>, the light absorption was significantly enhanced because of the resonant light trapping and light retrapping [41]. The extinction from 550 nm to 700 nm can be attributed to the light-scattering effect by the Au-bottom. As shown in the photographs (Fig. 3c), bare BiVO<sub>4</sub>/WO<sub>3</sub> on FTO with light green color seems to be transparent, due to its ultrathin in nature. In comparison, BiVO<sub>4</sub>/WO<sub>3</sub> on Au NSs is semi-transparent because a substantial portion of the light was absorbed and reflected by the Au NSs, while BiVO<sub>4</sub>/WO<sub>3</sub> on the Au-bottom is non-transparent, meaning that nearly all the light was absorbed and reflected. After coating with small surface Au NSs, the light absorption of Au-surface/BiVO<sub>4</sub>/WO<sub>3</sub>/Au-bottom was further



increased, and the broad absorption peak near 525 nm was also further enhanced, which indicated there was a coupling effect of electromagnetic field created by both of the Au nanostructures. The absorption spectra demonstrate that this special antenna/spacer/reflector nano-patterned structure can increase the total transport pathway of photons within the semiconductor layer and enhance the light absorption of the ultrathin BiVO<sub>4</sub> photoanode. Moreover, the band absorption edge shifted to longer wavelengths, indicating the antenna/spacer/reflector structure can extend the light absorption range via the LSPR effects.

The PEC performances of the prepared photoanodes were characterized by measuring the photocurrent density–voltage ( $J-V$ ) curve and wavelength dependent incident photocurrent conversion efficiency (IPCE) with a three-electrode PEC system in aqueous 0.5 M sodium sulfate (Na<sub>2</sub>SO<sub>4</sub>) solution without any hole scavenger (pH = 6.5). Fig. 4b is a set of chopped sweep  $J-V$  curves obtained from the above five photoanodes. The photocurrent of bare BiVO<sub>4</sub> was 0.31 mA/cm<sup>2</sup> at 1.23 V<sub>RHE</sub>, while, BiVO<sub>4</sub>/WO<sub>3</sub> exhibits higher photocurrent density (0.56 mA/cm<sup>2</sup> at 1.23 V<sub>RHE</sub>) compared to the bare BiVO<sub>4</sub>, due to the efficient charge separation originating from the formation of a type-II heterojunction of BiVO<sub>4</sub> with WO<sub>3</sub>, as reported previously [20,28]. After coating small Au NSs (Au-surface) on BiVO<sub>4</sub>/WO<sub>3</sub>, the photocurrent was enhanced to 0.91 mA/cm<sup>2</sup>, which was 62.5% higher than that of BiVO<sub>4</sub>/WO<sub>3</sub> without Au-surface. By integrating the Au-bottom underneath BiVO<sub>4</sub>/WO<sub>3</sub>, the photocurrent was further enhanced to 1.04 mA/cm<sup>2</sup>, which was 85.7% higher than that of BiVO<sub>4</sub>/WO<sub>3</sub>. More interestingly, by integrating the Au-bottom and Au-surface simultaneously, the photocurrent of Au-surface/BiVO<sub>4</sub>/WO<sub>3</sub>/Au-bottom achieved to as high as 1.31 mA/cm<sup>2</sup>, which was 133.9% higher than that of BiVO<sub>4</sub>/WO<sub>3</sub>, and 3.23 times higher than that of bare BiVO<sub>4</sub> obtained at the same potential. Additionally, after integrating the Au-surface, the onset potential ( $V_{\text{onset}}$ ) exhibited a significant negative shift, implying that both the charge transport and transfer as well as the recombination of electrons and holes were improved due to the combined plasmonic enhancement.

Fig. 5a shows the IPCEs measured at 1.23 V<sub>RHE</sub> for the above photoanodes in the range of 300–550 nm, which demonstrate a similar trend as the  $J-V$  results. The onset of IPCE for bare BiVO<sub>4</sub> photoanode is observed near 520 nm, which is consistent with the band edge shown in the light absorption spectra (Fig. 4a). After integrating the Au-bottom or Au-surface, the photoanodes combined with plasmonic Au structures showed consistently higher IPCE value compared to BiVO<sub>4</sub>/WO<sub>3</sub> photoanode. In particular, the Au-surface/BiVO<sub>4</sub>/WO<sub>3</sub>/Au-bottom photoanode outperforms the other four photoanodes. To demonstrate this plasmonic enhancement, the IPCE curves in the range of 300–700 nm were compared between the Au-surface/BiVO<sub>4</sub>/WO<sub>3</sub>/Au-bottom and

BiVO<sub>4</sub>/WO<sub>3</sub>. As shown in Fig. 5b, the Au-surface/BiVO<sub>4</sub>/WO<sub>3</sub>/Au-bottom photoanode exhibited consistently higher IPCE value than BiVO<sub>4</sub>/WO<sub>3</sub> over the entire measured wavelength range (300–700 nm). As shown in the enlarged view of the IPCE curves (inset of Fig. 5b), the onset of IPCE for BiVO<sub>4</sub>/WO<sub>3</sub> was near 520 nm, while the Au-surface/BiVO<sub>4</sub>/WO<sub>3</sub>/Au-bottom photoanode demonstrated a significant IPCE enhancement in the range of 525–700 nm.

To evaluate the kinetics of charge transfer in this antenna/spacer/reflector nanostructured photoanode system, electrochemical impedance spectroscopy (EIS) measurements were carried out. Fig. 6a shows the EIS spectra measured under 1 sun irradiation at 1.23 V<sub>RHE</sub> in a frequency range of 100 kHz–0.1 Hz for BiVO<sub>4</sub>, BiVO<sub>4</sub>/WO<sub>3</sub>, Au-surface/BiVO<sub>4</sub>/WO<sub>3</sub>, BiVO<sub>4</sub>/WO<sub>3</sub>/Au-bottom, and Au-surface/BiVO<sub>4</sub>/WO<sub>3</sub>/Au-bottom. Nyquist plots of all samples were fitted to a simple equivalent circuit (inset of Fig. 6a), where  $R_s$  represents the series resistance,  $Q_1$  represents the constant phase element for the electrolyte/electrode interface, and  $R_{ct}$  represents the charge transfer resistance at the interface of electrode/electrolyte [28,46]. Thus, the diameter of a semi-circle in the plot is related to the value of charge transfer resistance ( $R_{ct}$ ) across the interface of electrode/electrolyte. The fitted values of  $R_{ct}$  were 3274, 824, 483, 418, and 331  $\Omega$  for BiVO<sub>4</sub>, BiVO<sub>4</sub>/WO<sub>3</sub>, Au-surface/BiVO<sub>4</sub>, BiVO<sub>4</sub>/WO<sub>3</sub>/Au-bottom, and Au-surface/BiVO<sub>4</sub>/WO<sub>3</sub>/Au-bottom, respectively. The largest  $R_{ct}$  for BiVO<sub>4</sub> indicates that the charge transfer characteristics of BiVO<sub>4</sub> are poor, which was decreased by forming the heterojunction with WO<sub>3</sub> layer. After integrating the small Au NSs,  $R_{ct}$  was further decreased. That means the LSPR-excited hot electrons of Au NSs can be easily injected into the CB of BiVO<sub>4</sub> because the energy of hot electrons is higher than the CB of BiVO<sub>4</sub> [47], while the holes were transferred from BiVO<sub>4</sub> to Au NSs and then to the electrolyte, which is much easier than charges transferring directly from BiVO<sub>4</sub> to the electrolyte (as shown in the energy diagram in Fig. 1b). The introduction of the Au-bottom also significantly decreased  $R_{ct}$ , indicating that the Au-bottom can be served as electron collector, which might promote the charge separation and transport, and consequently reduce the overall charge transfer resistance [41]. To further confirm this plasmonic effect for the promotion of the charge separation, Photoluminescence (PL) spectra of the above five samples were performed. Generally, the relatively lower PL intensity means the higher separation efficiency and the lower recombination rate of the photo-generated electron–hole pairs. As shown in Fig. 6b, the PL of BiVO<sub>4</sub>/WO<sub>3</sub> exhibits a weaker PL intensity compared with the bare BiVO<sub>4</sub>, due to the efficient charge separation originating from the type-II heterojunction of BiVO<sub>4</sub> with WO<sub>3</sub>. After integrating the Au-bottom or Au-surface, the PL intensities of all the photoanodes combined with plasmonic Au structures were further reduced, which means both of the

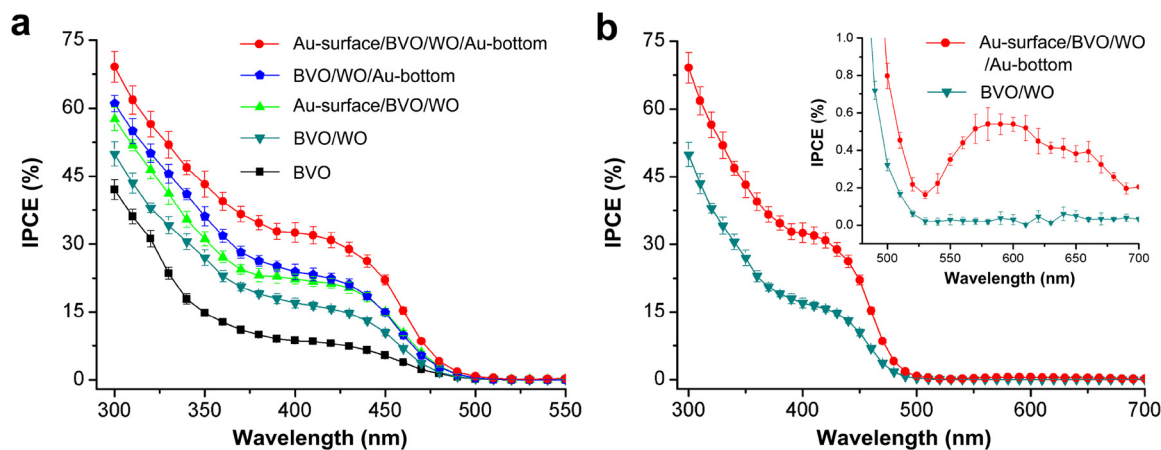


**Fig. 5.** IPCE of the different photoanodes. (a) IPCE curves measured at 1.23 V<sub>RHE</sub> for BiVO<sub>4</sub>, BiVO<sub>4</sub>/WO<sub>3</sub>, Au-surface/BiVO<sub>4</sub>/WO<sub>3</sub>, BiVO<sub>4</sub>/WO<sub>3</sub>/Au-bottom, and Au-surface/BiVO<sub>4</sub>/WO<sub>3</sub>/Au-bottom in the range of 300–550 nm. (b) IPCE curves measured at 1.23 V<sub>RHE</sub> for BiVO<sub>4</sub>/WO<sub>3</sub> and Au-surface/BiVO<sub>4</sub>/WO<sub>3</sub>/Au-bottom in the range of 300–700 nm. Inset figure in (b): enlarged view of the IPCE curves in (b) in the range of 475–700 nm.

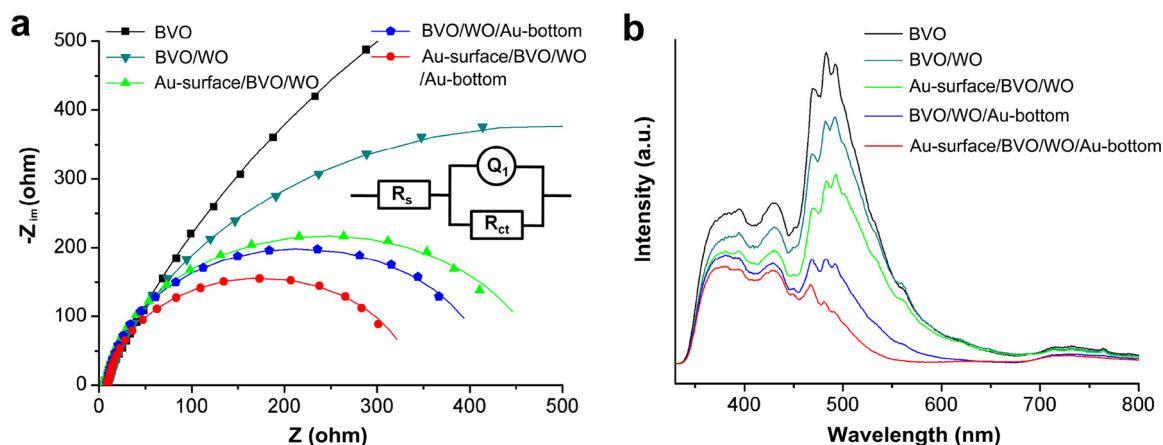


**Fig. 6.** EIS and PL spectra of the different photoanodes. (a) EIS curves measured at 1.23 V<sub>RHE</sub> for BiVO<sub>4</sub>, BiVO<sub>4</sub>/WO<sub>3</sub>, Au-surface/BiVO<sub>4</sub>/WO<sub>3</sub>, BiVO<sub>4</sub>/WO<sub>3</sub>/Au-bottom, and Au-surface/BiVO<sub>4</sub>/WO<sub>3</sub>/Au-bottom. (b) PL spectra of BiVO<sub>4</sub>, BiVO<sub>4</sub>/WO<sub>3</sub>, Au-surface/BiVO<sub>4</sub>/WO<sub>3</sub>, BiVO<sub>4</sub>/WO<sub>3</sub>/Au-bottom, and Au-surface/BiVO<sub>4</sub>/WO<sub>3</sub>/Au-bottom.

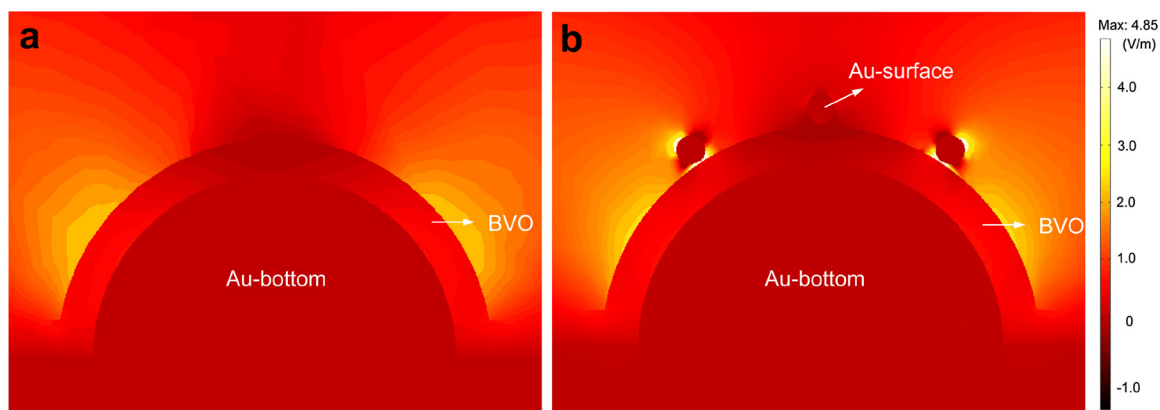


**Fig. 7.** Electric field distribution of the photoanodes at a wavelength of 550 nm. (a) Ultrathin BiVO<sub>4</sub> photoanode on the Au-bottom. (b) Ultrathin BiVO<sub>4</sub> photoanode between the Au-bottom and Au-surface.

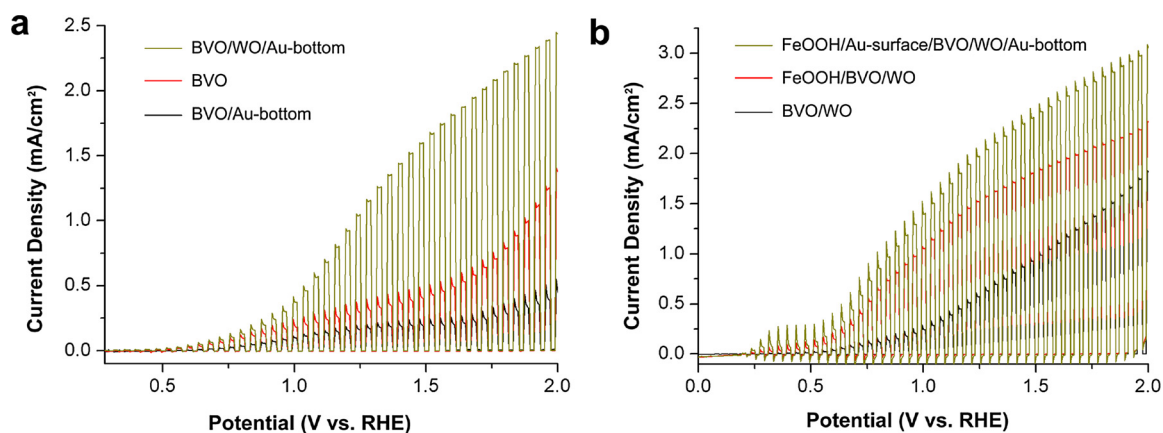


**Fig. 8.** *J*–*V* curves of the different photoanodes. (a) *J*–*V* curves measured under chopped light (AM 1.5G) in 0.5 M Na<sub>2</sub>SO<sub>4</sub> solution of BiVO<sub>4</sub>/Au-bottom, BiVO<sub>4</sub>, and BiVO<sub>4</sub>/WO<sub>3</sub>/Au-bottom. (b) *J*–*V* curves measured under chopped light (AM 1.5G) in 0.5 M Na<sub>2</sub>SO<sub>4</sub> solution of bare BiVO<sub>4</sub>/WO<sub>3</sub>, FeOOH/BiVO<sub>4</sub>/WO<sub>3</sub>, and FeOOH/Au-surface/BiVO<sub>4</sub>/WO<sub>3</sub>/Au-bottom.

Au-bottom and Au-surface can effectively promote the charge separation and suppress the charge recombination.

To understand the origin of the plasmonic enhancement from these two kinds of Au NSs, we try to explain the mechanisms from two aspects of the light manipulation and harvesting, and the enhanced electromagnetic field effects. First, this special antenna/spacer/reflector structure can increase the total transport pathway of photons within the

semiconductor layer, as indicated by the above light absorption results. The size of the plasmonic metal is one of the most important factors affecting light absorption and scattering properties [33,34]. As shown in Fig. 1a, the large (~245 nm) Au NSs combined with the Au film (Au-bottom) can scatter the incident light in the backward direction as a reflector. Therefore, integration of BiVO<sub>4</sub> onto the nanopatterned Au-bottom not only increases the surface roughness factor but also enables

the implementation of a dual light trapping strategy, resonant light trapping and light retrapping. For the small ( $\sim 20$  nm) Au NSs decorated on the BiVO<sub>4</sub> surface, the light-absorption effect dominates, compared to the light-scattering effect, which enables light harvesting of both the incident and reflected light from the Au-bottom. Therefore, these antenna/spacer/reflector structures can concentrate the light energy in the spacer (BiVO<sub>4</sub> layer) and promote light harvesting and absorption of BiVO<sub>4</sub>. Second, the origin of the photoactivity enhancements in plasmonic effects can be explained with the enhanced electromagnetic field effects of the two kinds of Au NSs. Plasmonic NPs have high capabilities for light trapping and electromagnetic field enhancement due to the collective oscillation of the free electrons on metal surface. The collective oscillation of electrons results in an enhanced local electromagnetic field, which is also known as LSPR [31,33]. To show the enhanced electromagnetic field of metal nanostructures under incident light, finite element modeling (FEM) analysis was carried out.

FEM modeling and calculation were performed for the antenna/spacer/reflector photoanodes under electromagnetic irradiation with wavelength of 550 nm in vacuum. The photoanodes were placed horizontally and parallel to the *xy* plane, while the incident light was along the *z* axis. The diameters of large and small Au NSs were defined as 245 and 20 nm, respectively. The thickness of the bottom Au film and BiVO<sub>4</sub> were 100 and 40 nm, respectively. The relative dielectric constant, electrical conductivity, and relative magnetic permeability of Au and BiVO<sub>4</sub> were shown in Table S1. Continuous boundary condition was set on all of the interfaces between vacuum space and the structures. After solving Maxwell equation, the two-dimensional electric field  $E(xz)$  amplitude can be calculated to describe the plasmonic enhancement at location (*xz*). As shown in Fig. 7, a strongly enhanced electric field was created by the nanopatterned Au-bottom, which was mainly confined near the Au-spheres surface (Fig. 7a). After the integration of small Au NSs, the electric field was further enhanced due to the strong coupling effect of the electromagnetic field created by both Au nanostructures (Fig. 7b). Therefore, a favorable interplay between the reflector and antennas has been created in the spacer (BiVO<sub>4</sub> layer) between Au-bottom and Au-surface, which is also known as hot spot. Similar metal-spacer-metal sandwich structures have demonstrated promising characteristics for surface-enhanced Raman scattering and infrared spectroscopy applications [30,42]. The enhanced electric field can promote the optical absorption and charge separation for BiVO<sub>4</sub> photoanodes.

It should be noted that the WO<sub>3</sub> layer (between the BiVO<sub>4</sub> layer and Au-bottom) serves as a selective electron transport layer because of the large valence band offset between WO<sub>3</sub> and BiVO<sub>4</sub>, which blocks the hole injection into the Au-bottom film and, therefore, reduces the interfacial charge recombination [46]. As shown in Fig. 8a, the photocurrent density of the BiVO<sub>4</sub> photoanode directly coated on the Au-bottom was much lower than that of the BiVO<sub>4</sub>/WO<sub>3</sub>/Au-bottom, and even lower than that of bare BiVO<sub>4</sub>, because the holes can easily transport from the valence band of BiVO<sub>4</sub> of the Au substrates. Moreover, a type-II heterojunction formed at the interface of WO<sub>3</sub> and BiVO<sub>4</sub> due to their suitable band alignment and band gap energies, which further improved the charge separation and transport (Fig. 1b). Therefore, the thin WO<sub>3</sub> layer also plays an important role in the antenna/spacer/reflector structure.

The PEC performance of the ultrathin BiVO<sub>4</sub> photoanode located between the plasmonic antennas and reflector could be further improved by coupling with OER catalysts. FeOOH, one of the most promising OER catalysts, was directly deposited on top of BiVO<sub>4</sub> photoanodes by a simple modified hydrothermal method. Fig. 8b demonstrates that the photocurrent density of BiVO<sub>4</sub>/WO<sub>3</sub> reaches 1.51 mA/cm<sup>2</sup> at 1.23 V<sub>RHE</sub> after the deposition of FeOOH, which is 1.70 times higher than that of the sample without FeOOH. Moreover, after the deposition of FeOOH, the photocurrent density of Au-surface/BiVO<sub>4</sub>/WO<sub>3</sub>/Au-bottom achieved 1.97 mA/cm<sup>2</sup> at 1.23 V<sub>RHE</sub>.

Finally, the PEC performance of the as-prepared Au-surface/BiVO<sub>4</sub>/

WO<sub>3</sub>/Au-bottom photoanode was compared to those of the BiVO<sub>4</sub> photoanodes reported in the literature (Table S2). It should be noted that pure BiVO<sub>4</sub> without doping was used in this work, and all of the PEC measurements were performed in the electrolyte of 0.5 M Na<sub>2</sub>SO<sub>4</sub> aqueous solution without any hole scavenger. The control samples of BiVO<sub>4</sub> and BiVO<sub>4</sub>/WO<sub>3</sub> showed low photocurrent density values, which were similar to those of the reported BiVO<sub>4</sub> photoanodes. However, the Au-surface/BiVO<sub>4</sub>/WO<sub>3</sub>/Au-bottom demonstrated a significantly enhanced photocurrent density, which was comparable or even better than the most of pure BiVO<sub>4</sub> films without doping in a typical thickness range of 200–500 nm.

#### 4. Conclusion

In summary, we reported an antenna/spacer/reflector based Au/BiVO<sub>4</sub>/Au nanopatterned photoanode by integrating ultrathin BiVO<sub>4</sub> layer between two kinds of Au NSs with different sizes for plasmon-enhanced PEC water splitting. The Au NSs with different sizes possess quite different light absorption and scattering properties. The large underlying Au NSs were used as the back reflector to reflect the incident light, while the small surface Au NSs on BiVO<sub>4</sub> photoanode acted as antennas for the absorption of the incident and reflected light. Therefore, these antenna/spacer/reflector structures concentrated the light energy in the BiVO<sub>4</sub> spacer layer and promoted the light harvesting and absorption of BiVO<sub>4</sub>. Moreover, a strong electromagnetic field was created in the BiVO<sub>4</sub> spacer due to the coupling interaction between the reflector and antenna, which promoted the charge separation and transport of BiVO<sub>4</sub>. As a result, the Au/BiVO<sub>4</sub>/Au nanopatterned photoanode demonstrated an impressive 3.23 fold enhancement on the photocurrent density at 1.23 V<sub>RHE</sub> and a significant negative shift of onset potential by the combined plasmonic effects. Significantly, the ultrathin BiVO<sub>4</sub> photoanode of only 70 nm thick achieved a photocurrent density of 1.31 mA/cm<sup>2</sup> at 1.23 V<sub>RHE</sub>, and it was further increased to 1.97 mA/cm<sup>2</sup> by coating FeOOH catalyst, which is comparable or even better than the most of the pure BiVO<sub>4</sub> films (200 nm or thicker) in the literature. This antenna/spacer/reflector based Au/BiVO<sub>4</sub>/Au photoanode can be further enhanced by optimizing the sizes of both Au NSs and the thickness of the BiVO<sub>4</sub> and WO<sub>3</sub> layers, and introducing impurity doping to further improve the charge transport efficiency. We believe that our antenna/spacer/reflector nanostructure and the corresponding plasmonic enhancement mechanism can be broadly applied to other semiconductors (e.g., Fe<sub>2</sub>O<sub>3</sub> and TiO<sub>2</sub>) and other thin-film optoelectronic devices (e.g., photovoltaic cells and electronics) for enhanced performance.

#### Acknowledgement

This work was supported by the National Research Foundation of Korea (NRF-2016R1A4A1010735).

#### Appendix A. Supplementary data

Supplementary material related to this article can be found, in the online version, at doi:<https://doi.org/10.1016/j.apcatb.2018.06.048>.

#### References

- [1] A. Landman, H. Dotan, G.E. Shter, M. Wullenkord, A. Houaijia, A. Maljusch, G.S. Grader, A. Rothschild, Photoelectrochemical water splitting in separate oxygen and hydrogen cells, *Nat. Mater.* 16 (2017) 646–652.
- [2] J.B. Sambur, T.Y. Chen, E. Choudhary, G.Q. Chen, E.J. Nissen, E.M. Thomas, N.M. Zou, P. Chen, Sub-particle reaction and photocurrent mapping to optimize catalyst-modified photoanodes, *Nature* 530 (2016) 77–80.
- [3] A. Fujishima, K. Honda, Electrochemical photolysis of water at a semiconductor electrode, *Nature* 238 (1972) 37–38.
- [4] S. Kim, T. Kim, S. Lee, S. Baek, T. Park, K. Yong, A highly versatile and adaptable artificial leaf with floatability and planar compact design applicable in various natural environments, *Adv. Mater.* 29 (2017) 1702431.



- [5] Y.C. Qiu, K.Y. Yan, H. Deng, S.H. Yang, Secondary branching and nitrogen doping of ZnO nanotetrapods: building a highly active network for photoelectrochemical water splitting, *Nano Lett.* 12 (2012) 407–413.
- [6] Z. Zhang, M. Choi, M. Baek, Z.X. Deng, K.J. Yong, Plasmonic and passivation effects of Au decorated RGO/CdSe nanofilm uplited by CdSe@ZnO nanorods with photoelectrochemical enhancement, *Nano Energy* 21 (2016) 185–197.
- [7] Q.Y. Zeng, J.H. Li, J. Bai, X.J. Li, L.G. Xia, B.X. Zhou, Preparation of vertically aligned WO<sub>3</sub> nanoplate array films based on peroxotungstate reduction reaction and their excellent photoelectrocatalytic performance, *Appl. Catal. B: Environ.* 202 (2017) 388–396.
- [8] J.J. Zhang, P. Zhang, T. Wang, J.L. Gong, Monoclinic WO<sub>3</sub> nanomultilayers with preferentially exposed (002) facets for photoelectrochemical water splitting, *Nano Energy* 11 (2015) 189–195.
- [9] J.S. Luo, L. Steier, M.K. Son, M. Schreier, M.T. Mayer, M. Gratzel, Cu<sub>2</sub>O nanowire photocathodes for efficient and durable solar water splitting, *Nano Lett.* 16 (2016) 1848–1857.
- [10] H.W. Gao, C. Liu, H.E. Jeong, P.D. Yang, Plasmon-enhanced photocatalytic activity of iron oxide on gold nanopillars, *ACS Nano* 6 (2012) 234–240.
- [11] J.T. Li, S.K. Cushing, P. Zheng, F.K. Meng, D. Chu, N.Q. Wu, Plasmon-induced photonic and energy-transfer enhancement of solar water splitting by a hematite nanorod array, *Nat. Commun.* 4 (2013) 2651.
- [12] P.Y. Kuang, L.Y. Zhang, B. Cheng, J.G. Yu, Enhanced charge transfer kinetics of Fe<sub>2</sub>O<sub>3</sub>/CdS composite nanorod arrays using cobalt-phosphate as cocatalyst, *Appl. Catal. B: Environ.* 218 (2017) 570–580.
- [13] T.W. Kim, K.S. Choi, Nanoporous BiVO<sub>4</sub> photoanodes with dual-layer oxygen evolution catalysts for solar water splitting, *Science* 343 (2014) 990–994.
- [14] Y.M. Ma, A. Kafizas, S.R. Pendlebury, F. Le Formal, J.R. Durrant, Photoinduced absorption spectroscopy of CoPi on BiVO<sub>4</sub>: the function of CoPi during water oxidation, *Adv. Funct. Mater.* 26 (2016) 4951–4960.
- [15] S.C. Wang, P. Chen, J.H. Yun, Y.X. Hu, L.Z. Wang, An electrochemically treated BiVO<sub>4</sub> photoanode for efficient photoelectrochemical water splitting, *Angew. Chem. Int. Ed.* 56 (2017) 8500–8504.
- [16] L.G. Xia, J. Bai, J.H. Li, Q.Y. Zeng, L.S. Li, B.X. Zhou, High-performance BiVO<sub>4</sub> photoanodes cocatalyzed with an ultrathin  $\alpha$ -Fe<sub>2</sub>O<sub>3</sub> layer for photoelectrochemical application, *Appl. Catal. B: Environ.* 204 (2017) 127–133.
- [17] Y. Hou, Z.H. Wen, S.M. Cui, X.L. Feng, J.H. Chen, Strongly coupled ternary hybrid aerogels of N-deficient porous graphitic-C<sub>3</sub>N<sub>4</sub> nanosheets/N-doped graphene/NiFe-layered double hydroxide for solar-driven photoelectrochemical water oxidation, *Nano Lett.* 16 (2016) 2268–2277.
- [18] H. Zhang, J.H. Kim, J.H. Kim, J.S. Lee, Engineering highly ordered iron titanate nanotube array photoanodes for enhanced solar water splitting activity, *Adv. Funct. Mater.* 27 (2017) 1702428.
- [19] L.L. Cai, J.H. Zhao, H. Li, J. Park, I.S. Cho, H.S. Han, X.L. Zheng, One-step hydrothermal deposition of Ni:FeOOH onto photoanodes for enhanced water oxidation, *ACS Energy Lett.* 1 (2016) 624–632.
- [20] P.M. Rao, L.L. Cai, C. Liu, I.S. Cho, C.H. Lee, J.M. Weiss, P.D. Yang, X.L. Zheng, Simultaneously efficient light absorption and charge separation in WO<sub>3</sub>/BiVO<sub>4</sub> core/shell nanowire photoanode for photoelectrochemical water oxidation, *Nano Lett.* 14 (2014) 1099–1105.
- [21] L.T. Zhou, C.Q. Zhao, B. Giri, P. Allen, X.W. Xu, H. Joshi, Y.Y. Fan, L.V. Titova, P.M. Rao, High light absorption and charge separation efficiency at low applied voltage from Sb-doped SnO<sub>2</sub>/BiVO<sub>4</sub> core/shell nanorod-array photoanodes, *Nano Lett.* 16 (2016) 3463–3474.
- [22] B. Zhang, H.P. Zhang, Z.Y. Wang, X.Y. Zhang, X.Y. Qin, Y. Dai, Y.Y. Liu, P. Wang, Y.J. Li, B.B. Huang, Doping strategy to promote the charge separation in BiVO<sub>4</sub> photoanodes, *Appl. Catal. B: Environ.* 211 (2017) 258–265.
- [23] S. Singh, R. Sharma, G. Joshi, J.K. Pandey, Formation of intermediate band and low recombination rate in ZnO-BiVO<sub>4</sub> heterostructured photocatalyst: investigation based on experimental and theoretical studies, *Korean J. Chem. Eng.* 34 (2017) 500–510.
- [24] D.K. Zhong, S. Choi, D.R. Gamelin, Near-complete suppression of surface recombination in solar photoelectrolysis by “Co-Pi” catalyst-modified W:BiVO<sub>4</sub>, *J. Am. Chem. Soc.* 133 (2011) 18370–18377.
- [25] J.S. Yang, J.J. Wu, Low-potential driven fully-depleted BiVO<sub>4</sub>/ZnO heterojunction nanodendrite array photoanodes for photoelectrochemical water splitting, *Nano Energy* 32 (2017) 232–240.
- [26] X.J. Shi, Y. Choi, K. Zhang, J. Kwon, D.Y. Kim, J.K. Lee, S.H. Oh, J.K. Kim, J.H. Park, Efficient photoelectrochemical hydrogen production from bismuth vanadate-decorated tungsten trioxide helix nanostructures, *Nat. Commun.* 5 (2014) 4775.
- [27] M. Zhou, J. Bao, Y. Xu, J.J. Zhang, J.F. Xie, M.L. Guan, C.L. Wang, L.Y. Wen, Y. Lei, Y. Xie, Photoelectrodes based upon Mo: BiVO<sub>4</sub> inverse opals for photoelectrochemical water splitting, *ACS Nano* 8 (2014) 7088–7098.
- [28] S.J. Hong, S. Lee, J.S. Jang, J.S. Lee, Heterojunction BiVO<sub>4</sub>/WO<sub>3</sub> electrodes for enhanced photoactivity of water oxidation, *Energy Environ. Sci.* 4 (2011) 1781–1787.
- [29] S.H. Yoon, D.W. Park, K.S. Kim, Preparation of WO<sub>3</sub>, BiVO<sub>4</sub> and reduced graphene oxide composite thin films and their photoelectrochemical performance, *Korean J. Chem. Eng.* 34 (2017) 3220–3225.
- [30] Y.R. Fang, Y. Jiao, K.L. Xiong, R. Ogier, Z.J. Yang, S.W. Gao, A.B. Dahlin, M. Kall, Plasmon enhanced internal photoemission in antenna-spacer-mirror based Au/TiO<sub>2</sub> nanostructures, *Nano Lett.* 15 (2015) 4059–4065.
- [31] X.Z. Zheng, L.W. Zhang, Photonic nanostructures for solar energy conversion, *Energy Environ. Sci.* 9 (2016) 2511–2532.
- [32] B. Chen, G.W. Meng, Q. Huang, Z.L. Huang, Q.L. Xu, C.H. Zhu, Y.W. Qian, Y. Ding, Green synthesis of large-scale highly ordered core@shell nanoporous Au@Ag nanorod arrays as sensitive and reproducible 3D SERS substrates, *ACS Appl. Mater. Interfaces* 6 (2014) 15667–15675.
- [33] P. Zhang, T. Wang, J.L. Gong, Mechanistic understanding of the plasmonic enhancement for solar water splitting, *Adv. Mater.* 27 (2015) 5328–5342.
- [34] A. Tcherniak, J.W. Ha, S. Dominguez-Medina, L.S. Slaughter, S. Link, Probing a century old prediction one plasmonic particle at a time, *Nano Lett.* 10 (2010) 1398–1404.
- [35] Y.C. Pu, G.M. Wang, K.D. Chang, Y.C. Ling, Y.K. Lin, B.C. Fitzmorris, C.M. Liu, X.H. Lu, Y.X. Tong, J.Z. Zhang, Y.J. Hsu, Y. Li, Au nanostructure-decorated TiO<sub>2</sub> nanowires exhibiting photoactivity across entire UV-visible region for photoelectrochemical water splitting, *Nano Lett.* 13 (2013) 3817–3823.
- [36] X.M. Zhang, Y.L. Chen, R.S. Liu, D.P. Tsai, Plasmonic photocatalysis, *Rep. Prog. Phys.* 76 (2013) 046401.
- [37] S.K. Cushing, J.T. Li, F.K. Meng, T.R. Senty, S. Suri, M.J. Zhi, M. Li, A.D. Bristow, N.Q. Wu, Photocatalytic activity enhanced by plasmonic resonant energy transfer from metal to semiconductor, *J. Am. Chem. Soc.* 134 (2012) 15033–15041.
- [38] H. Dotan, O. Kfir, E. Sharlin, O. Blank, M. Gross, I. Dumchin, G. Ankonina, A. Rothschild, Resonant light trapping in ultrathin films for water splitting, *Nat. Mater.* 12 (2013) 158–164.
- [39] S. Mubeen, J. Lee, N. Singh, S. Kramer, G.D. Stucky, M. Moskovits, An autonomous photosynthetic device in which all charge carriers derive from surface plasmons, *Nat. Nanotechnol.* 8 (2013) 247–251.
- [40] R. Xu, L.Y. Wen, Z.J. Wang, H.P. Zhao, S.P. Xu, Y. Mi, Y. Xu, M. Sommerfeld, Y.G. Fang, Y. Lei, Three-dimensional plasmonic nanostructure design for boosting photoelectrochemical activity, *ACS Nano* 11 (2017) 7382–7389.
- [41] J.H. Zhao, Y. Guo, L.L. Cai, H. Li, K.X.Z. Wang, I.S. Cho, C.H. Lee, S.H. Fan, X.L. Zheng, High-performance ultrathin BiVO<sub>4</sub> photoanode on textured polydimethylsiloxane substrates for solar water splitting, *ACS Energy Lett.* 1 (2016) 68–75.
- [42] F. Neubrech, C. Huck, K. Weber, A. Pucci, H. Giessen, Surface-enhanced infrared spectroscopy using resonant nanoantennas, *Chem. Rev.* 117 (2017) 5110–5145.
- [43] D.D. Men, F. Zhou, L.F. Hang, X.Y. Li, G.T. Duan, W.P. Cai, Y. Li, A functional hydrogel film attached with a 2D Au nanosphere array and its ultrahigh optical diffraction intensity as a visualized sensor, *J. Mater. Chem. C* 4 (2016) 2117–2122.
- [44] X.H. Ji, X.N. Song, J. Li, Y.B. Bai, W.S. Yang, X.G. Peng, Size control of gold nanocrystals in citrate reduction: the third role of citrate, *J. Am. Chem. Soc.* 129 (2007) 13939–13948.
- [45] J.Y. Kim, D.H. Youn, K. Kang, J.S. Lee, Highly conformal deposition of an ultrathin FeOOH layer on a hematite nanostructure for efficient solar water splitting, *Angew. Chem. Int. Ed.* 55 (2016) 10854–10858.
- [46] S. Byun, B. Kim, S. Jeon, B. Shin, Effects of a SnO<sub>2</sub> hole blocking layer in a BiVO<sub>4</sub>-based photoanode on photoelectrocatalytic water oxidation, *J. Mater. Chem. A* 5 (2017) 6905–6913.
- [47] L.W. Zhang, C.Y. Lin, V.K. Valev, E. Reisner, U. Steiner, J.J. Baumberg, Plasmonic enhancement in BiVO<sub>4</sub> photonic crystals for efficient water splitting, *Small* 10 (2014) 3970–3978.